OPTICS

Low-threshold parametric oscillation in organically modified microcavities

Xiaoqin Shen,[1]* Rigoberto Castro Beltran,[2,3] Vinh M. Diep,[1] Soheil Soltani,[3] Andrea M. Armani[1,3]*

Coherent frequency generators are an enabling platform in basic science and applied technology. Originally reliant on high-power lasers, recently comb generation has been demonstrated in ultrahigh-*Q* microcavities. The large circulating intensity within the cavity results in strong light-matter interaction, giving rise to Kerr parametric oscillations for comb generation. However, the comb generation threshold is limited by competing nonlinear effects within the cavity material and low intrinsic material Kerr coefficients. We report a new strategy to fabricate near-infrared frequency combs based on combining high-*Q* microcavities with monomolecular layers of highly nonlinear small molecules. The functionalized microcavities demonstrate high-efficiency parametric oscillation in the near-IR and generate primary frequency combs with 0.88-mW thresholds, improving optical parametric oscillation generation over nonfunctionalized devices by three orders of magnitude. This organic-inorganic approach enables otherwise unattainable performance and will inspire the next generation of integrated photonic device platforms.

INTRODUCTION

Optical frequency comb generators are of great interest in many areas, such as frequency metrology (*1*), high-precision spectroscopy (*2*, *3*), and quantum information processing (*4*). A common strategy for generating frequency combs is to leverage a four-wave mixing (FWM)–based optical parametric oscillation (OPO) process, which is induced by the Kerr nonlinearity in a crystalline optical material. In this process, two pump photons (ω_p) are converted to a pair of signal (ω_s) and idler (ω_i) photons that are symmetric to the pump frequency (*5*). If the OPO process is highly efficient and there are excess photons, then this process can generate additional sidebands through secondary mixing processes, thus resulting in comb generation.

To achieve a sufficient concentration of photons for the FWM process to occur, the original comb systems used high-power lasers to excite crystalline materials with large Kerr coefficients in a long optical cavity (*1*, *6*–*8*). During the past decade, researchers have significantly advanced the field by replacing the high-power lasers with integrated photonic microdevices capable of amplifying the input optical field. This strategy has significantly reduced the complexity and size of these systems (*9*–*11*). This device-driven approach has focused on improving the optical performance or the quality factor (*Q*) of the device, which governs the amplification ability.

Ultrahigh-*Q* whispering-gallery mode microresonators are particularly suited to act as comb generators. The ultrahigh *Q* ensures high-circulating optical intensities within the resonator, reducing the threshold power needed to generate nonlinear phenomena. These devices have been fabricated from a wide range of dielectric and semiconductor materials (*12*–*14*). Nearly all have demonstrated frequency comb generation and other nonlinear behaviors (*11*, *13*–*15*).

Typically, a FWM process is leveraged to achieve comb generation in a microcavity. This process requires that the ultrahigh-*Q* cavity is fabricated from a material with a high third-order nonlinear coefficient and low dispersion. The parametric FWM process is enhanced if the signal and idler frequencies coincide with optical modes of the cavity (*16*). When the scattering rate into the signal and idler modes exceeds their respective optical cavity decay rates, OPO occurs (*14*). OPO in the microcavity leads to the generation of additional lines that contain multiple pairwise equidistant sidebands, spaced by the multiple free spectral ranges of the cavity. This multistage process results in the formation of the frequency comb.

To realize OPO in microcavities, the detuning $\Delta\omega$ should be sufficiently small ($\Delta\omega \approx 0$) for phase matching to occur (*9*). In addition, $\Delta\omega$ is required to be less than the parametric gain bandwidth $\Omega = 4\,\frac{n_2}{n}\frac{\omega}{A_{\text{eff}}}P$, where P is the pump power, n_2 is the optical Kerr coefficient, and n is the linear refractive index (*17*). Therefore, to achieve OPO and comb generation, it is necessary to operate within these boundary conditions, placing fundamental limits on device design. Unfortunately, nonparametric processes follow many of the same design guidelines and requirements, making it difficult to isolate a single nonlinear process (*16*, *18*).

In addition, the inorganic materials that are available to fabricate high-*Q* microresonators generally exhibit small intrinsic third-order nonlinear coefficients, often resulting in multiple nonlinear optical (NLO) effects in parallel (*16*, *18*, *19*). For example, in addition to parametric processes, nonparametric processes, such as stimulated Raman scattering (SRS) (*20*–*22*), can also be easily excited in these devices. In SiO_2, the optical Kerr coefficient of silica is six orders of magnitude smaller than the Raman gain coefficient ($n_2 = 2.2 \times 10^{-20}$ m^2/W compared to $g_R = 0.66 \times 10^{-13}$ m/W). As a result, even under ideal operating conditions, the theoretical threshold value of OPO in a silica device is very close to that of SRS (*5*, *16*), leading to the concurrence of the two processes. This challenge is not isolated to silica. The performance of high-*Q* resonators made of other materials, such as CaF_2, diamond, and silicon, also suffer from the same competition between stimulated Raman emission and comb generation (*18*, *19*, *23*). The competing processes can negatively affect the frequency conversion efficiency and output purity (*5*, *18*).

An emerging class of highly NLO materials is based on organic conjugated molecules. These materials can be designed to have high second- or third-order nonlinearities superior to common inorganic amorphous or crystalline materials (*24*). Extensive organic NLO

[1]Mork Family Department of Chemical Engineering and Materials Science, University of Southern California, Los Angeles, CA 90089, USA. [2]Departamento de Ingeniería Física, División de Ciencias e Ingenierías, Campus Léon, Universidad de Guanajuato, Léon, México. [3]Ming Hsieh Department of Electrical Engineering-Electrophysics, University of Southern California, Los Angeles, CA 90089, USA.
*Corresponding author. Email: xiaoqins@usc.edu (X.S.); armani@usc.edu (A.M.A.)

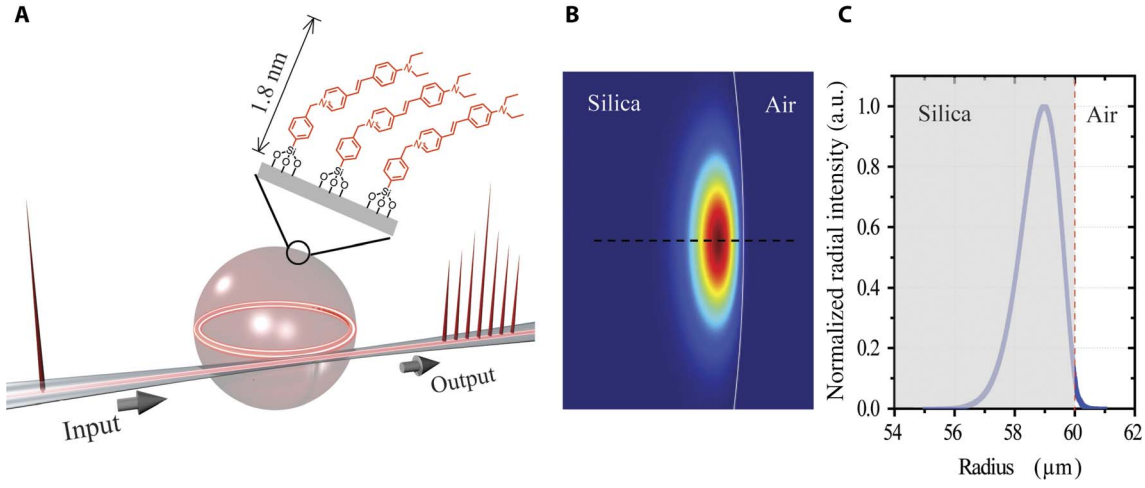

Fig. 1. Surface functionalizaton of the silica microcavities. (**A**) Rendering of the silica optical microcavity with a nanolayer of oriented NLO molecules on the surface. The microcavity is shown coupled to a waveguide and on resonance. In this condition, the input optical field is amplified, resulting in comb generation. The oriented and aligned nanolayer is approximately 1.8 nm in length. (**B**) FEM simulation of the optical mode profile in the microcavity with a radius of 60 μm. The white line indicates the boundary between the silica device and the environment (air). (**C**) The mode profile at the cross section of the device indicated by the dashed black line in (B) verifies that about 1% of the optical field extends into the environment and is able to interact with the DASP monomolecular layer on surface. In addition, the presence of the ultrathin monolayer does not change or distort the optical mode profile or the effective mode area (A_{eff}) of the microcavities. a.u., arbitrary units.

molecules have been synthesized and studied (*25*), driven by their promise in nonlinear optics applications, such as all optical switching (*26*), electro-optic modulation (*27*), and two-photon absorption (*28*). More recently, efforts have been made to develop organic molecules with large Kerr nonlinear coefficients (*29*). However, because of fundamental incompatibilities with conventional nanofabrication methods, limited success has been realized in the development of a cavity-based frequency comb using these materials.

Here, we functionalize the surface of ultrahigh-*Q* optical microcavities with an NLO monomolecular layer to achieve high-efficiency parametric oscillation and to generate primary frequency combs in the near-infrared. Here, we focus on the small molecule 4-[4-diethylamino(styryl)]pyridinium (DASP). However, the fundamental concept of leveraging oriented monolayers of highly nonlinear small molecules to enhance device performance is broadly translatable to other integrated optical devices.

RESULTS AND DISCUSSION

The surface of the silica microcavities is functionalized with a single layer of small molecules having a very high third-order nonlinear coefficient. The DASP molecules [$n_{2(DASP)} = 2.54 \times 10^{-17}$ m^2/W] are covalently bound to the silica surface, forming an ultrathin and oriented monomolecular layer of approximately 1.8 nm, corresponding to the molecular length (Fig. 1A) (*30*). Finite element method (FEM) modeling of the optical mode profile was performed to determine the interaction of the optical field with the small-molecule monolayer (see the Supplementary Materials). The simulations show that approximately 1% of the optical field is located in the evanescent tail (Fig. 1C). Thus, it is expected that the optical cavity can directly and efficiently interact with the monolayer. The effective mode area (A_{eff}) and the effective refractive index of the microcavities are not changed by the presence of the ultrathin (<2 nm) monolayer.

On the basis of these results, this ultrathin layer does not distort or disturb the optical mode profile in a step-like manner but instead alters the environment in a more subtle manner, allowing an effective medium model to be used. This behavior is particularly important because it indicates that the same circulating optical mode can experience both material systems simultaneously. Hence, the monolayer would serve to increase the Kerr gain of the silica in proportion to the optical mode overlap with both material systems. Given this overlap, an enhancement in the FWM process is expected because the combined Kerr coefficient, $(1 - k)n_{2(silica)} + kn_{2(DSAP)}$, is calculated to be 27.6×10^{-20} m^2/W, which is 10 times higher than that of silica (k is the percentage of optical evanescent field in the second material).

The surface of the silica microcavities was functionalized with DASP using a two-step molecular self-assembly method (Fig. 2A). The formation of the molecular monolayers was characterized by x-ray photoelectron spectroscopy (XPS; Fig. 2B). The high-resolution XPS spectrum of the DASP-grafted silica clearly shows a binding energy peak at 398.2 eV from N, confirming the formation of the DASP molecular layer on the surface. To further verify the DASP monolayer on the device surface, we imaged the fluorescence of DASP using fluorescence microscopy (Fig. 2C). The DASP-functionalized microcavity shows uniform fluorescence, confirming the successful attachment of the DASP layer to the device (figs. S1 and S2).

The impact of the DASP monomolecular layer on the optical *Q* was determined at each step in the functionalization process using a set of five devices. Details on the measurement setup are in the Supplementary Materials (fig. S3). As shown in Fig. 3, the initial silica and silanated microcavities exhibited ultrahigh-*Q* values averaging 1×10^8 at 1550 nm, whereas the DASP-functionalized silica hybrid microcavities showed slightly lower *Q* values but still in the 10^7 to 10^8 range. *Q* values above 10^7 ensure efficient excitation of the organic monolayers. The ability to maintain *Q* values in this range is only possible because the precision of the grafting process resulted in minimal scattering and contamination loss as well as minimal damage to the device surface.

The emission spectra for nonfunctionalized ($Q = 1.0 \times 10^8$) and DASP-functionalized microcavities ($Q = 0.7 \times 10^8$) pumped with a 1550-nm laser were characterized using an optical spectrum analyzer (OSA). The emission spectra over a range of input powers were recorded to determine both the lasing threshold and efficiency. Additional measurement details are in the Supplementary Materials (fig. S1).

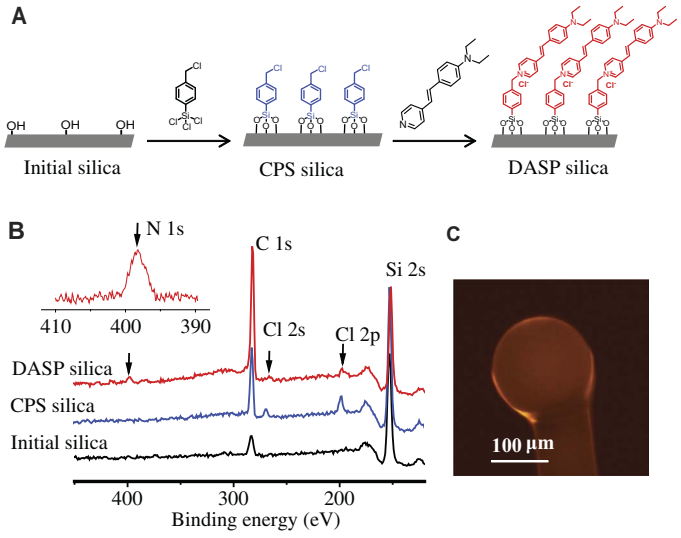

Fig. 2. Surface functionalization and characterization of the microcavities. (**A**) Schematic of the surface functionalization process. Benzyl chloride silane is attached to the silica surface using silanization chemistry. The DASP molecule is then attached via a quaternization reaction, forming an oriented monolayer. (**B**) XPS spectra of nonfunctionalized silica, chloromethylphenylsilane (CPS)–functionalized silica, and DASP-functionalized silica. The peak binding energy at about 200 eV is the primary peak of Cl(2p) from the CPS molecules of the CPS-functionalized silica. The additional binding energy peak at about 400 eV is due to the nitrogen from the grafted DASP molecule of the DASP-functionalized silica. Inset: A high-resolution XPS spectrum of the DASP-grafted silica, clearly showing a binding energy peak at 398.2 eV from nitrogen. (**C**) Fluorescence image of a DASP-functionalized microcavity (excitation at 403 nm and emission from 565 to 615 nm using a band-pass filter). By leveraging the fluorescence of DASP, the DASP monolayer on the device surface is directly imaged using fluorescence microscopy.

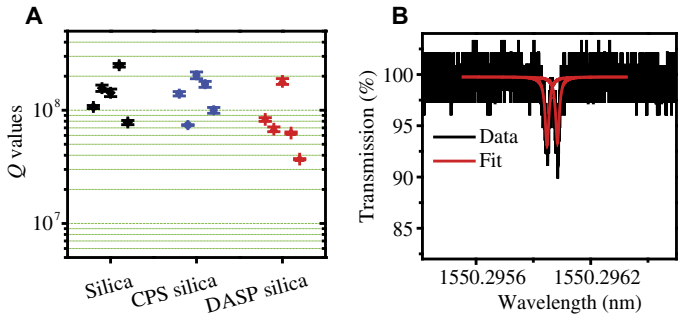

Fig. 3. Intrinsic *Q* values of the hybrid optical microcavities. (**A**) *Q* values of a set of five devices measured at 1550 nm at each step in the functionalization process. (**B**) Typical transmission spectrum of a DASP-functionalized silica microcavity. By fitting the spectra to a Lorentzian and using the expression $Q = \lambda/\delta\lambda$, where $\delta\lambda$ is the full width at half maximum (FWHM), the loaded *Q* of the device was calculated to be 0.7×10^8.

In the nonfunctionalized silica microcavities, no apparent signal/idler photon pairs centered at 1550 nm were observed over the power range tested (Fig. 4A). Instead, SRS around 1655 nm dominates the output spectra, as previously reported in silica microcavities (*31*–*33*).

In contrast, in the DASP-functionalized microcavities, signal/idler photon pairs with equal output power centered at 1550 nm appeared first at sub-mW input powers (Fig. 4B). Moreover, even at high-input powers, no other emission peaks in the detection wavelength range were observed. Changes in the *Q* value of the DASP-functionalized device did not change this behavior (fig. S4).

The observed preferential behavior for OPO exhibited by the microcavity can be understood by evaluating the relative threshold power required for SRS and OPO. Specifically, by equating the parametric and Raman thresholds in a resonator under critical coupling, a figure-of-merit parameter can be established: $\xi \approx 1.54 \frac{\lambda_P}{2\pi} \frac{g_R}{n_2}$, where λ_P is the pump wavelength, g_R is the Raman gain coefficient, and n_2 is the Kerr coefficient (Supplementary Materials) (*5*, *17*). In a binary hybrid system, the g_R and n_2 of the small-molecule layer must be included, resulting in a slight modification to this expression: $\xi \approx 1.54 \frac{\lambda_P}{2\pi} \frac{2g_{R,silica}}{(1-k)n_2 + kn_2'}$, where $g_{R,silica}$ is the Raman gain coefficient of silica and k is the percentage of optical evanescent field in the material (by definition, $k < 1$).

Assuming a fixed device geometry, this expression allows different nonlinear regimes to be established. When $\xi > 1$, the Raman threshold is lower than the parametric threshold, and SRS is preferred. When $\xi \approx 1$, OPO and SRS will coexist. When $\xi < 1$, the parametric threshold is lower than the Raman threshold, and OPO is preferred. The ξ value of the DASP-silica device was calculated to be 0.48, indicating that OPO is preferred in these devices. In addition, because of the high Kerr nonlinearity of the surface DASP molecules [$n_{2(DASP)} = 2.54 \times 10^{-17}$ m^2/W] compared to that of silica [$n_{2(silica)} = 2.2 \times 10^{-20}$ m^2/W], in the DASP-functionalized silica microcavities, the effective parametric gain bandwidth (Ω_{DS}) of the devices was estimated to be approximately one order of magnitude larger than that of nonfunctionalized silica (Ω_{silica}). The significant enhancement in parametric gain bandwidth ensures that the condition for FWM is fulfilled: $\Omega_{DS} \gg \Delta\omega$. Therefore, only parametric oscillation occurs in the DASP-functionalized hybrid microcavities, resulting in the observed preferential generation of OPO with no Raman emission lines present.

To more quantitatively determine the performance improvement due to the small-molecule layer, the threshold for the DASP-functionalized device can be compared to the silica device (Fig. 5). Primary frequency combs with a spacing of ~3.8 nm were observed with multiple secondary signal/idler photons (Fig. 5A). This spacing agrees with the calculated free spectral range of the silica cavity, which is 3.82 nm for the 138-µm diameter device. This agreement is notable because it indicates that the optical mode in the DASP-functionalized microcavity is not distorted by the addition of an ultrathin monomolecular layer. The output power of the signal/idler photon pairs increases markedly with increasing input pump power. The parametric oscillation threshold value of the DASP-functionalized device ($Q = 0.7 \times 10^8$) is 0.88 mW (Fig. 5B). Above the threshold, the FWM process shows a cubic dependence (slope, 3.1) of the first generated idler output power on the input power (fig. S5). Because the Kerr coefficient experienced by the optical field is increased by the DASP monolayer, the parametric oscillation process is also significantly enhanced compared to a conventional silica microcavity. For comparison, the measured maximum output power of the DASP-functionalized device is three orders of magnitude higher than that of a nonfunctionalized device (Fig. 5B).

CONCLUSION

In conclusion, we have demonstrated a materials-driven strategy to generate low-threshold frequency combs in organic-silica hybrid microcavities by removing parasitic secondary nonlinear effects. To verify our approach, we used a self-assembly method to graft small molecules with

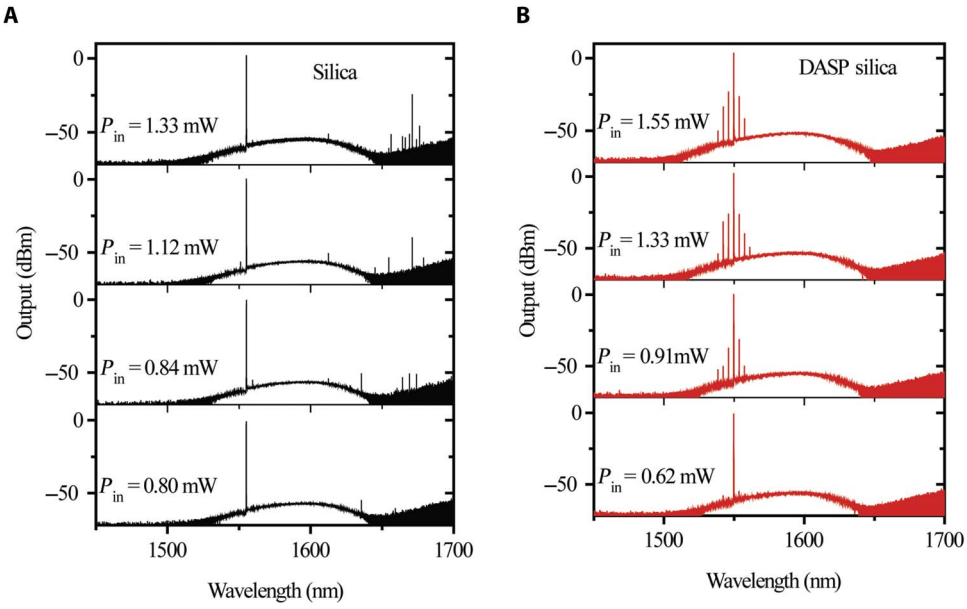

Fig. 4. Representative output spectra from the hybrid microcavities. Output spectra of (**A**) nonfunctionalized and (**B**) DASP-functionalized microcavities with similar *Q* values (1.0×10^8 and 0.7×10^8, respectively) pumped by a 1550-nm continuous-wave (CW) diode laser under different input power (P_{in}) values.

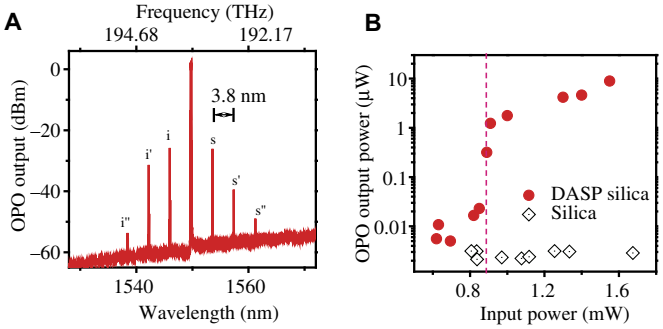

Fig. 5. Comparison of OPO behaviors in different microcavities. (**A**) Representative primary Kerr comb from DASP-functionalized hybrid microcavities pumped at 1550 nm, with a spacing of ~3.8 nm (0.46 THz). (**B**) Output power in the first generated idler photon as a function of peak intensity in cavities of a DASP-functionalized silica microcavity with $Q = 0.7 \times 10^8$ and a nonfunctionalized silica with $Q = 1.0 \times 10^8$. The OPO threshold for DASP-functionalized silica microcavity was observed to be 0.88 mW, whereas a clear threshold value was not observed within the same experimental input power range for a nonfunctionalized silica microcavity.

large Kerr coefficients on the surface of optical resonators. As a result of the precision of the monolayer formation, the ultrahigh-*Q* values of the devices are minimally affected. The large Kerr coefficients of the DASP molecular monolayers significantly increased the overall Kerr nonlinearity of the device, enhancing the OPO by three orders of magnitude, compared to the nonfunctionalized microcavities. This work represents a unique strategy using organic molecules to generate frequency combs in ultrahigh-*Q* cavities. This approach is not limited to the specific optical microcavity material or device geometry used in the present work but is broadly applicable to any optical resonant cavity platform. Thus, the strategy demonstrated here provides a universal approach for optimizing integrated photonic devices with novel functionalities. The combination of highly nonlinear organic molecules with integrated nanophotonics opens the door to a wide range of organic-hybrid photonic technologies for frequency combs (*1*, *34*), ultrafast optical modulations (*35*), all-optical switching (*36*), and quantum information processing (*4*).

MATERIALS AND METHODS

General information

Reagents and solvent were purchased from Sigma-Aldrich and used without further purification unless otherwise noted. [4-(Chloromethyl)phenyl]trichlorosilane (97%) was purified by distillation. 4-[4-Diethylamino(styryl)]pyridine was synthesized according to a reported procedure (*37*).

Device fabrication

The initial silica microcavities were fabricated from optical fiber (Newport) using a previously detailed method (*38*). Briefly, the polymer cladding was removed, the fiber end-face was cleaved and cleaned, and the fiber was exposed to a carbon dioxide laser. The final device diameters were approximately 120 μm.

DASP-silica surface functionalization

The initial silica microcavities were first treated by O_2 plasma to generate dense hydroxyl groups on the silica surface. Then, the [4-(chloromethyl)phenyl]trichlorosilane coupling agent was deposited on the surface of the plasma-treated silica spheres using chemical vapor deposition at room temperature for 8 min, yielding a CPS-grafted microcavities.

A 4-[4-diethylamino(styryl)]pyridine solution in chloroform was first drop-casted onto the CPS-grafted microcavities to form a uniform, oriented layer of 4-[4-diethylamino(styryl)]pyridine. Then, the coated devices were heated to 110°C under vacuum for 20 min. The devices were cooled to room temperature, rinsed thoroughly with chloroform and acetone, and dried under vacuum at 110°C for 2 min, yielding a grafted DASP layer on the surface.

FEM simulation

The simulation procedure explained in the literature was used to perform the simulation (*39*). Briefly, we drew a cross section of the resonator and solved Maxwell's equations by assuming an axially symmetric mode. We chose the mesh size to be λ/8 to have an acceptable accuracy. Once the software solves for the optical modes, we drew lines on the equatorial plane of the resonator and calculated the electric field magnitude for all three components of the field (E_{axial}, $E_{azimuthal}$, and E_{radial}). Using the geometries and material properties defined by the experiments, we performed FEM modeling of the optical mode profile to determine the interaction of the optical field with the small-molecule monolayer. We showed a cross section of the fundamental mode along with the field amplitude profile on the equatorial plane. In addition, the presence of the monolayer did not change or distort the optical mode profile. Thus, it is expected that the optical cavity can directly and efficiently interact with the monolayer. In addition, the effective mode area (A_{eff}) and the effective refractive index of the microcavities were not changed by the presence of the ultrathin (<2 nm) monolayer.

Optical testing

To measure *Q*, light from a 1550-nm narrow-linewidth tunable CW diode laser was evanescently coupled into and out of the microcavities using a tapered optical fiber waveguide. The coupling efficiency was optimized by controlling the distance between the tapered waveguide and the microcavities using a three-dimensional nanopositioning stage. The output signal was split, with one portion going to an oscilloscope and the other going to an OSA. Transmission spectra were recorded on the oscilloscope, and the *Q* was calculated by fitting the spectra to a Lorentzian and using the expression $Q = \lambda/\delta\lambda$, where δλ is the FWHM determined for the fit. *Q* factor measurements were performed in the undercoupled regime.

To characterize the emission behavior of the device, the amount of power coupled into the device was increased until critical coupling was achieved. The emission spectra were recorded on the OSA over a range of input powers from below threshold to well-above threshold. Additional details are in the Supplementary Materials.

SUPPLEMENTARY MATERIALS

Supplementary material for this article is available at http://advances.sciencemag.org/cgi/content/full/4/1/eaao4507/DC1

section S1. Surface functionalization characterization
section S2. Device characterization
section S3. Theoretical justification for ξ
fig. S1. Absorption and emission spectra of the DASP molecule.
fig. S2. Fluorescence and bright-field images of the microspheres.
fig. S3. Measurement scheme.
fig. S4. Two representative output spectra of DASP-functionalized silica microspheres with different *Q* factors pumped at 1550 nm.
fig. S5. Power dependence of the first generated idler photon above threshold, showing a cubic dependency (slope is 3.1) of the first generated idler output power on input power.
fig. S6. Two representative output spectra of nonfunctionalized silica microspheres with different *Q* factors pumped at 1550 nm.

REFERENCES AND NOTES

1. T. Udem, R. Holzwarth, T. W. Hänsch, Optical frequency metrology. *Nature* **416**, 233–237 (2002).
2. G. Millot, S. Pitois, M. Yan, T. Hovhannisyan, A. Bendahmane, T. W. Hänsch, N. Picqué, Frequency-agile dual-comb spectroscopy. *Nat. Photonics* **10**, 27–30 (2016).
3. B. Lomsadze, S. T. Cundiff, Frequency comb-based four-wave-mixing spectroscopy. *Opt. Lett.* **42**, 2346–2349 (2017).
4. C. Reimer, M. Kues, P. Roztocki, B. Wetzel, F. Grazioso, B. E. Little, S. T. Chu, T. Johnston, Y. Bromberg, L. Caspani, D. J. Moss, R. Morandotti, Generation of multiphoton entangled quantum states by means of integrated frequency combs. *Science* **351**, 1176–1180 (2016).
5. I. H. Agha, Y. Okawachi, M. A. Foster, J. E. Sharping, A. L. Gaeta, Four-wave-mixing parametric oscillations in dispersion-compensated high-*Q* silica microspheres. *Phys. Rev. A* **76**, 043837 (2007).
6. W. Liang, D. Eliyahu, V. S. Ilchenko, A. A. Savchenkov, A. B. Matsko, D. Seidel, L. Maleki, High spectral purity Kerr frequency comb radio frequency photonic oscillator. *Nat. Commun.* **6**, 7957 (2015).
7. D. J. Jones, S. A. Diddams, J. K. Ranka, A. Stentz, R. S. Windeler, J. L. Hall, S. T. Cundiff, Carrier-envelope phase control of femtosecond mode-locked lasers and direct optical frequency synthesis. *Science* **288**, 635–639 (2000).
8. M. Vainio, L. Halonen, Stabilization of femtosecond optical parametric oscillators for infrared frequency comb generation. *Opt. Lett.* **42**, 2722–2725 (2017).
9. M. A. Foster, A. C. Turner, J. E. Sharping, B. S. Schmidt, M. Lipson, A. L. Gaeta, Broad-band optical parametric gain on a silicon photonic chip. *Nature* **441**, 960–963 (2006).
10. S.-W. Huang, J. Yang, M. Yu, B. H. McGuyer, D.-L. Kwong, T. Zelevinsky, C. W. Wong, A broadband chip-scale optical frequency synthesizer at 2.7×10^{-16} relative uncertainty. *Sci. Adv.* **2**, e1501489 (2016).
11. R. Castro-Beltrán, V. M. Diep, S. Soltani, E. Gungor, A. M. Armani, Plasmonically enhanced Kerr frequency combs. *ACS Photonics* **4**, 2828–2834 (2017).
12. D. Chen, A. Kovach, X. Shen, S. Poust, A. M. Armani, On-chip ultra-high-*Q* silicon oxynitride optical resonators. *ACS Photonics* **4**, 2376–2381 (2017).
13. X. Lu, J. Y. Lee, S. Rogers, Q. Lin, Optical Kerr nonlinearity in a high-Q silicon carbide microresonator. *Opt. Express* **22**, 30826–30832 (2014).
14. T. J. Kippenberg, R. Holzwarth, S. A. Diddams, Microresonator-based optical frequency combs. *Science* **332**, 555–559 (2011).
15. X. Jiang, L. Shao, S.-X. Zhang, X. Yi, J. Wiersig, L. Wang, Q. Gong, M. Lončar, L. Yang, Y.-F. Xiao, Chaos-assisted broadband momentum transformation in optical microresonators. *Science* **358**, 344–347 (2017).
16. A. B. Matsko, A. A. Savchenkov, D. Strekalov, V. S. Ilchenko, L. Maleki, Optical hyperparametric oscillations in a whispering-gallery-mode resonator: Threshold and phase diffusion. *Phys. Rev. A* **71**, 033804 (2005).
17. T. J. Kippenberg, S. M. Spillane, K. J. Vahala, Kerr-nonlinearity optical parametric oscillation in an ultrahigh-*Q* toroid microcavity. *Phys. Rev. Lett.* **93**, 083904 (2004).
18. Y. K. Chembo, I. S. Grudinin, N. Yu, Spatiotemporal dynamics of Kerr-Raman optical frequency combs. *Phys. Rev. A* **92**, 043818 (2015).
19. A. G. Griffith, M. Yu, Y. Okawachi, J. Cardenas, A. Mohanty, A. L. Gaeta, M. Lipson, Coherent mid-infrared frequency combs in silicon-microresonators in the presence of Raman effects. *Opt. Express* **24**, 13044 (2016).
20. P. Latawiec, V. Venkataraman, M. J. Burek, B. J. M. Hausmann, I. Bulu, M. Lončar, On-chip diamond Raman laser. *Optica* **2**, 924–928 (2015).
21. Y. Takahashi, Y. Inui, M. Chihara, T. Asano, R. Terawaki, S. Noda, A micrometre-scale Raman silicon laser with a microwatt threshold. *Nature* **498**, 470–474 (2013).
22. Y. Okawachi, M. Yu, V. Venkataraman, P. M. Latawiec, A. G. Griffith, M. Lipson, M. Lončar, A. L. Gaeta, Competition between Raman and Kerr effects in microresonator comb generation. *Opt. Lett.* **42**, 2786–2789 (2017).
23. N. Riesen, S. Afshar, A. François, T. M. Monro, Material candidates for optical frequency comb generation in microspheres. *Opt. Express* **23**, 14784–14795 (2015).
24. P. Günter, *Nonlinear Optical Effects and Materials* (Springer, 2012), vol. 72.
25. S. Barlow, S. R. Marder, Nonlinear optical properties of organic materials, in *Functional Organic Materials: Syntheses, Strategies and Applications*,T. J. J. Müller, U. H. F. Bunz, Eds. (Wiley-VCH Verlag GmbH and Co. KGaA, 2007), pp. 393–437.
26. C. Koos, P. Vorreau, T. Vallaitis, P. Dumon, W. Bogaerts, R. Baets, B. Esembeson, I. Biaggio, T. Michinobu, F. Diederich, W. Freude, J. Leuthold, All-optical high-speed signal processing with silicon–organic hybrid slot waveguides. *Nat. Photonics* **3**, 216–219 (2009).
27. L. R. Dalton, P. A. Sullivan, D. H. Bale, Electric field poled organic electro-optic materials: State of the art and future prospects. *Chem. Rev.* **110**, 25–55 (2010).
28. G. S. He, L.-S. Tan, Q. Zheng, P. N. Prasad, Multiphoton absorbing materials: Molecular designs, characterizations, and applications. *Chem. Rev.* **108**, 1245–1330 (2008).
29. J. M. Hales, J. Matichak, S. Barlow, S. Ohira, K. Yesudas, J.-L. Brédas, J. W. Perry, S. R. Marder, Design of polymethine dyes with large third-order optical nonlinearities and loss figures of merit. *Science* **327**, 1485–1488 (2010).
30. N. Peor, R. Sfez, S. Yitzchaik, Variable density effect of self-assembled polarizable monolayers on the electronic properties of silicon. *J. Am. Chem. Soc.* **130**, 4158–4165 (2008).
31. M. V. Chistiakova, A. M. Armani, Cascaded Raman microlaser in air and buffer. *Opt. Lett.* **37**, 4068–4070 (2012).
32. N. Deka, A. J. Maker, A. M. Armani, Titanium-enhanced Raman microcavity laser. *Opt. Lett.* **39**, 1354–1357 (2014).
33. X.-F. Jiang, Y.-F. Xiao, C.-L. Zou, L. He, C.-H. Dong, B.-B. Li, Y. Li, F.-W. Sun, L. Yang, Q. Gong, Highly unidirectional emission and ultralow-threshold lasing from on-chip ultrahigh-Q microcavities. *Adv. Mater.* **24**, OP260–OP264 (2012).
34. L. Razzari, D. Duchesne, M. Ferrera, R. Morandotti, S. Chu, B. E. Little, D. J. Moss, CMOS-compatible integrated optical hyper-parametric oscillator. *Nat. Photonics* **4**, 41–45 (2010).

35. X. Hu, P. Jiang, C. Ding, H. Yang, Q. Gong, Picosecond and low-power all-optical switching based on an organic photonic-bandgap microcavity. *Nat. Photonics* **2**, 185–189 (2008).
36. W. Yoshiki, T. Tanabe, All-optical switching using Kerr effect in a silica toroid microcavity. *Opt. Express* **22**, 24332–24341 (2014).
37. P. G. Lacroix, M. C. Munoz, A. B. Gaspar, J. A. Real, S. Bonhommeau, V. Rodriguez, K. Nakatanie, Synthesis, crystal structures, and solid state quadratic nonlinear optical properties of a series of stilbazolium cations combined with gold cyanide counter-ion. *J. Mater. Chem.* **21**, 15940–15949 (2011).
38. A. J. Maker, A. M. Armani, Fabrication of silica ultra high quality factor microresonators. *J. Vis. Exp.* e4164 (2012).
39. M. Oxborrow, Traceable 2-D finite-element simulation of the whispering-gallery modes of axisymmetric electromagnetic resonators. *IEEE Trans. Microw. Theory Tech.* **55**, 1209–1218 (2007).

Acknowledgments
Funding: The authors would like to acknowledge the Intelligence Advanced Research Projects Activity (2016-16070100002), the Office of Naval Research (N00014-11-1-0910), and the Northrop Grumman Institute of Optical Nanomaterials and Nanophotonics. **Author contributions:** X.S. conceived and performed the experiments and analyzed the data. R.C.B. and V.M.D. contributed to performing the experiments. S.S. carried out the simulations. A.M.A. supervised the project. X.S. and A.M.A. wrote the manuscript. All the authors commented on the manuscript. **Competing interests:** The authors declare that they have no competing interests. **Data and materials availability:** All data needed to evaluate the conclusions in the paper are present in the paper and/or the Supplementary Materials. Additional data related to this paper may be requested from the authors.

Submitted 21 July 2017
Accepted 29 November 2017
Published 5 January 2018
10.1126/sciadv.aao4507

Citation: X. Shen, R. C. Beltran, V. M. Diep, S. Soltani, A. M. Armani, Low-threshold parametric oscillation in organically modified microcavities. *Sci. Adv.* **4**, eaao4507 (2018).

Low-threshold parametric oscillation in organically modified microcavities

Xiaoqin Shen, Rigoberto Castro Beltran, Vinh M. Diep, Soheil Soltani and Andrea M. Armani

Sci Adv **4** (1), eaao4507.
DOI: 10.1126/sciadv.aao4507